Impact of DFT Properties on the Inherent Resolution of Compressed Sensing Reconstructed Images

Michael Smith[1], Jordan Woehr[2], Emily Marasco[3] and M Ethan MacDonald[4]

Department of Electrical and Computer Engineering[1-3], Seaman MR Centre[4]

University of Calgary, Calgary, Canada T2N 1N4

E-mail: ([1]smithmr, [2]jmwoehr, [3]eamarsco, [4]memacdon) @ucalgary.ca

Abstract − Compressed sensing (*CS*) algorithms exploit sparseness properties to reconstruct high spatial resolution magnetic resonance (*MR*) images from *k*-space data acquisitions significantly under sampled to reduce imaging times. *CS* algorithm effectiveness is frequently shown using under-sampled *k*-space data from *NxN* simulated images. These demonstration reconstructions are near perfect with quality higher than reconstructions using under-sampled *NxN* experimental *k*-space data sets. These differences are explained in terms of the interaction between the explicit transform domain sparsity requirement employed during iterative *CS* reconstruction and an inherent frequency domain property of the discrete Fourier transform (*DFT*). We report on experiments to overcome the limitations imposed by this *DFT* property by modifying the *CS* objective function to use a sparseness transform with a resolution higher that the standard transform related to the acquired *NxN* data matrix size. We demonstrate the relative effectiveness and limitations of standard *CS* and our proposed high-resolution *k*-space extrapolation enabled (*Hi-KEE*) *CS* reconstruction on under- and fully-sampled, simulated and experimental *MR k*-space data.

Keywords − Rapid imaging, compressed sensing image reconstruction, magnetic resonance images, image resolution confounding factors.

I INTRODUCTION

Partial Fourier reconstruction (*PFR*) was an early attempt to use incomplete *k*-space data to solve the conflicting requirements associated with acquiring a series of high-spatial resolution magnetic resonance (*MR*) images in a short period of time. Compressed sensing (*CS*) reconstruction techniques applied to under-sampled *k*-space data, *e.g.* [1], have recently received greater attention than the 1980's constrained reconstruction approaches, *e.g.* [2], as a solution to overcome the distortions resulting from *k*-space data that no longer meets the Shannon / Nyquist sampling criterion.

McGibney et al. [3] used the underlying digital signal processing (*DSP*) characteristics of algorithms to understand the relative limitations of *PFR* implementations; and proposed new reconstruction approaches. In this paper, we perform a similar analysis on *DSP* characteristics that might impact the available resolution from *CS*-reconstructed *MR*

images and lead to greater understanding of possible new algorithmic approaches.

The paper is formatted as follows. In the Theory section, the implications of Harris's work [4] on discrete Fourier transform *(DFT)* windows is re-examined in the context of *CS* reconstructions where *DFT*s are repeatedly used to move data between *k*-space and image domains. This reformulation reveals an implicit *DFT*-related *MR k*-space continuity property that can directly impact the effective resolution of individual high resolution components of the *CS* reconstructed image. We propose restoring the *CS* image resolution by using *Hi-KEE;* a high-resolution *k*-space extrapolation enabled variant of the *SPARSE-MRI* algorithm [1].

In the Method section, we use an *MR* Shepp-Logan phantom with increased high-resolution detail to demonstrate the impact of this inherent *DFT* property on the resolution of *CS* and *Hi-KEE* reconstructed images. The resolution of reconstructed *CS* images from a Shepp-Logan simulation study and experimental *MR k*-space data are shown in the Results

and Discussion section; followed by discussion of approaches to enhance the resolution of *CS* reconstructed images.

II THEORY

a) Description of simulated and experimental MR k-space data sets

The typical *NxN MR* image $I[x,y]_{EXPT}$; $-0 \leq x, y < N$ is the *IDFT* transformed k-space data set experimentally obtained by a *MR* scanner

$$S[k_x,k_y]_{EXPT} = S[k_x,k_y]; -N/2 \leq |k_x,k_y| < N/2; \qquad (1)$$

Van de Walle *et al.* [5] model *MR* data capture and image reconstruction through continuous and discrete transformations of an infinite spatial-frequency representation, $S(k_x,k_y)$; $-\infty < |k_x,k_y| < \infty$ of a high resolution (*HR*) object description with $I(x,y)$; $-\infty < |x,y| < \infty$ the corresponding continuous object-space image. Thus $S[k_x,k_y]_{EXPT}$ is derived by a truncation of an infinite matrix of values $S[k_x,k_y]$; $-\infty \leq |k_x,k_y| < \infty$ sampled from the original $S(k_x,k_y)$ representation. In this paper, round and square brackets are respectively used to distinguish between continuous, $S(k_x,k_y)$, and discrete, $S[k_x,k_y]$, variables.

To simplify further discussion, we approximate $S[k_x,k_y]_{EXPT}$ as the truncation

$$S[k_x,k_y]_{EXPT} = S[k_x,k_y]_{MNxMN}; -N/2 \leq |k_x,k_y| < N/2; \qquad (2)$$

of a finite, rather than infinite, k-space matrix $S[k_x,k_y]_{MNxMN}$; $MN \leq |k_x,k_y| < MN$ in the limit $MN \to \infty$. This allows us to express the description of the continuous object-space *MR* image in terms of a *HR* discrete *MNxMN* image with pixel intensities $I[x,y]_{MNxMN}$; $0 \leq x, y < MN$ with a corresponding *MNxMN HR* k-space data set:

$$S[k_x,k_y]_{MNxMN}$$
$$= \sum_{x,y} I[x,y]_{MNxMN} \exp(-2\pi k_x x/MN)\exp(-2\pi k_y y/MN);$$
$$- MN/2 \leq |k_x,k_y| < MN/2; \quad 0 \leq x, y < MN \qquad (3)$$

The $S[k_x,k_y]_{EXPT}$ samples in Eqn. (2) differ from those analytically derived directly in k-space from a *HR* object description as in Chartrand [6]. However, the differences between the sampled values of the two models become increasingly small for large

MN and concentrated around the k-space boundaries $|k_x,k_y| \approx MN/2$ (aliasing effects [4]) where the differences will be masked by the decreasing experimental k-space-to-noise ratio with increasing *k* [7]. If $M >> 1$, the differences between the experimental k-space values from the two models becomes increasing small for the experimental truncated *NxN* data values, $S[k_x,k_y]_{EXPT}$ captured by an MR imager.

With our simplified model, the experimental *NxN* k-space data, $S[k_x,k_y]_{EXPT}$, can be described in Van de Walle *et al.* [5] terms as: an *MNxMN-TO-NxN* transformation of the *MNxMN* image $I[x,y]_{MNxMN}$ to k-space accomplished through a *MNxMN* DFT operation ($M >> 1$), followed by a *NxN* k-space truncation.

This truncated data, $S[k_x,k_y]_{EXPT}$, Eqn. (2) is different from the $S[k_x,k_y]_{NxN}$ k-space values generated from the simulated *NxN* Shepp-Logan phantom image used in a number of papers discussing CS reconstruction effectiveness; *e.g.* the *SPARSE-MRI* software package demonstration of *CS* reconstruction effectiveness [1]. This phantom data can be described in terms of a direct *NxN-TO-NxN image-to-k-space* transformation accomplished through a *NxN* DFT operation performed on an *NxN* image $I[x,y]_{NxN}$; $0 \leq x, y < N$

$$S[k_x,k_y]_{NxN} = \sum_{x,y} I[x,y]_{NxN} \exp(-2\pi k_x x/N)\exp(-2\pi k_y y/N)$$
$$- N/2 \leq |k_x,k_y| < N/2; \quad 0 \leq x, y < N \qquad (5)$$

b) CS reconstruction basics

MR images can be successfully reconstructed with *CS* by solving the following optimization problem

$$\min \| \psi I_{CS}[] \|_1 \text{ such that } FI_{CS}[] = K_{NxN}[] \qquad (6)$$

where
- the proposed imaging trajectory to acquire the under-sampled *NxN* k-space data $K_{NxN}[]$ generates incoherent (noise-like) aliasing artefacts in the image;
- a sparse representation, $\psi I_{CS}[]$, of the reconstructed image, $I_{CS}[]$, is known to exist in a transform domain; and
- the enforcement of sparsity during image reconstruction, *i.e.* minimizing the L1-norm $\| \psi I_{CS}[] \|_1$, occurs while maintaining consistency between the known under-sampled k-space data $K_{NxN}[]$ and the under-sampled k-space data $FI_{CS}[]$ derived from the

CS reconstructed image by the partial Fourier operator F [1].

c) Interpreting Harris Observations in CS context

Current CS algorithms [1] make extensive use of transforms between *k*-space and a sparse image domain. In principle there may be advantages if such transforms were performed analytically on continuous descriptions of the *MR* data, but the *DFT* must be used in practice. Harris [4] discusses the differences between pixels of the discretely sampled image, $I[x,y]_{ICFT}$, derived from the inverse continuous Fourier transform *(ICFT), $I(x,y)$*, of a continuous signal, $S(k_x,k_y)$, and pixels of the image generated by applying the *IDFT* to a limited sub-set of sampled values, $S[k_x,k_y]$, derived from the continuous *k*-space signal. Harris [4] demonstrated that a key factor in the equivalence of discretized *ICFT* and the *IDFT* values of *MR* image pixels was linked to the *NxN* cyclic periodicity implicitly imposed on the real and imaginary components of the truncated MRI *k*-space data matrix through use of the *IDFT* during reconstruction.

Harris [4] also demonstrates that finite length data sets with cyclic continuity in their amplitude have lower amplitudes present in the ringing surrounding a main peak in the other domain (the side lobes associated with spatial or spectral leakage) compared to data with no cyclic continuity. Additional levels of cyclic continuity further reduces the ringing, e.g. amplitude and first derivative continuity. This implicit cyclic continuity is associated with the end points of the finite data sequences that comprise any cross-section of the *NxN* *k*-space matrix used during *MR* image reconstruction; e.g. the continuity between $S[k_{x1},k_y]$ and $S[k_{x2},k_y]$ where $k_{x1}=N/2-1$ and $k_{x2}=-N/2$.

Re-interpreting the Harris' observations implies that any truncated *MR* *k*-space data that possesses *NxN* cyclic periodic properties will be automatically appear more sparse (no side lobes) following any *NxN* transformation that involves the *DFT* algorithm than would data without *NxN* cyclic periodicity. We describe such data as being inherently *NxN* sparse. We hypothesize such *NxN* sparse data would be more easily recovered from an under-sampled set of *k*-space data during *CS* reconstruction on a *NxN* grid than data without *NxN* cyclic periodicity, i.e. data that is not inherently *NxN* sparse.

The components of the *k*-space signal $S[k_x,k_y]_{NxN}$ from the *NxN* phantom, Eqn. (5), are complex exponential basis functions belonging to an *NxN* discrete space. By definition, these components are *NxN* cyclically continuous in amplitude and in all *N-1* derivatives. We identify this data as being inherently *NxN* sparse in a *CS* context as each *k*-space cross-section exponential component will be individually transformed to a single image-space pixel. By comparison, Van de Walle's description [5] of the experimental MR signal indicates that $S[k_x,k_y]_{EXPT}$, Eqn. (2), is derived from an *MNxMN* sparse signal, Eqn. (3). Only the original high resolution image $I[x,y]_{MNxMN}$ components located at positions where the ratios *x/M* and *y/M* are integers will generate inherently *NxN* sparse *k*-space components following the *NxN* truncation.

The *SPARSE-MRI* software *CS* reconstruction [1] demonstration generates a near-perfect image from under-sampled *k*-space values, $S[k_x,k_y]_{NxN}$, of a *NxN* Shepp-Logan phantom. Here the optimization problem expressed in Eqn. (6) is expressed in terms of minimizing the *CS* objective function, the sum of L1 norms in *NxN* unity transform and total variation domains, with the constraint that the L2 norm of the difference between the under sampled measured *NxN* data and the solution does not exceed some estimated noise amount. We hypothesize that the perfect reconstruction is associated with the inherent *NxN* sparseness of the $S[k_x,k_y]_{NxN}$ values; and that only those components of an experimental $S[k_x,k_y]_{EXPT}$ data set that are also inherently *NxN* sparse will similarly be ideally reconstructed.

We suggest that requiring the image be sparse following an *NxN* transform during *CS* reconstruction can be re-interpreted in terms of suppression of the side-lobes of the main signal components. We therefore hypothesize that application of the *NxN* sparsity transform will impose cyclic continuity on the reconstructed non-inherently *NxN* sparse *k*-space data components where none existed before; leading to a resolution change relative to the *NxN* sparse data components. We suggest changing the standard *CS* objective function involving a *NxN* sparsity transform related to the measured data size to a *PNxPN* sparsity transform more closely associated with the *MNxMN* *HR* resolution of the original image. We hypothesize that the *CS* resolution for non *NxN* sparse components of the truncated experimental *MR* data set would improve when the *DFT* imposed *k*-space cyclic characteristics are shifted from $|k_x,k_y|\approx N/2$ to $|k_x,k_y|\approx PN/2;\quad P>1$.

III METHOD

The standard MATLAB Shepp-Logan phantom script *Phantom( ),* (MATLAB, R2011a, The Math-Works, Natick, MA, USA) was modified as *Modi-*

fiedPhantom( ) to use a high resolution image description, *HiResObject*, Fig. 1A. The high resolution features present in the new phantom image included an under-sized variant of the standard Shepp-Logan phantom modified to provide varying, rather than constant, wall thicknesses. In addition (i) *NxN* sparse features were generated by centring fine lines at locations $x = vM; 0 \leq v < N$ for all vertical line features in the left upper image and the first line in the left lower image of Fig. 1A; and (ii) the remaining lower left lines centred at $x \neq vM$ to produce non *NxN* sparse features.

Simulated data generation method 1 (SDG-M1):
The call *ModifiedPhantom(N)* produced the image $I[x, y]_{NxN}$, Fig. 1E. Following a 2D *DFT,* this became $S[k_x, k_y]_{NxN}$, Fig. 1D. This is the equivalent of the *NxN* k-space data set used in [1] and other papers when demonstrating the success of *CS* reconstruction algorithms.

Simulated data generation method 2 (SDG-M2):
The call *ModifiedPhantom(MN)* produced Fig. 1A; a *MNxMN* image, $I[x, y]_{MNxMN}$ with image resolution *FOV / MN,* where *FOV* is the field of view of the object, *M = 32* and *N = 64*. This underwent a *MNxMN-TO-MNxMN image-to-k-space* transformation before being truncated to size *NxN* to produce the simulated experimental *MR* data set $S[k_x, k_y]_{EXPT}$, Eqn. (3), Fig. 1B. Application of a 2D *IDFT* produced the experimental image, $I[x, y]_{EXPT}$, Fig. 1C.

a) Experiments performed

Small under-sampled *64x64* k-space data sets were prepared using SDG-M1 and SDG-M2 generation approaches to simulate the application of *CS* reconstruction to achieve high-temporal resolution *MR* image sequences during *fMRI*. These simulated reconstructions were compared to those of a truncated *64x64* experimental k-space data set derived from a *512x512* raw k-space *MRI* experimental scan of a GE phantom. The experimental scan used a fast gradient recalled echo sequence, FOV of 18cm^2, slice thickness of 6 mm and TR / TE / flip values of 7.5 ms / 3.7 ms / 20^0 respectively.

A basic premise behind this paper is to identify approaches to remove unrecognized issues with existing *CS* reconstruction implementations rather than proposing new algorithms. The software settings for the *SPARSE- MRI* demonstration package (www.eecs.berkeley.edu/mlustig/software/ sparse-MRI_v0.2.tar.gz) were left unchanged with (A) the
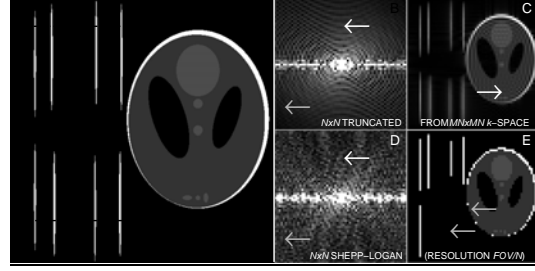

Fig. 1. (A) The modified HR Shepp-Logan, resolution *FOV / MN*, can be transformed into k-space and truncated (B) to size *MNxMN* to mimic MR acquisition. This leads to image (C) following IDFT reconstruction. Many *CS* reconstruction evaluations directly generate a Shepp-Logan phantom image (E) at a resolution *FOV / N* [1] before DFT transformation to produce the simulated k-space data set (D). Differences in k-space data sets (B) and (D) include regional changes in regularity (white arrow) and amplitude (grey arrow). Image differences include ringing artefacts (white arrow in C) and loss of fine detail (grey arrows in E).

use of the identity transform, and (B) k-space under-sampling levels representing a cross-section of a *3D* data set fully sampled in the k_z direction with a 33% random k_x and k_y sampling scheme, centre core of size 0.1. These data sets were then reconstructed using the standard *NxN* grid. The *HI-KEE CS* reconstruction algorithm was implemented by presenting an under-sampled *NxN* k-space data set padded with zeros to size *PNxPN* to the *SPARSE-MRI* software set to generate a high resolution *PNxPN* reconstruction. Lustig et al. [1] discusses how certain *NxN* k-space under-sampling schemes produce point-spread functions that better matched the *CS* requirement of generating incoherent (noise-like) aliasing artefacts in the transformed image. This study was repeated using cross-sections of only the fine vertical lines from Fig. 1A to explore the point spread functions generated by *CS* reconstruction of under-sampled k-space data sets that included a combination of *NxN* sparse and non-*NxN* sparse components.

IV RESULTS AND DISCUSSION

a)   SDG-M1 and SDG-M2 k-space differences

The properties of the *DFT* [4] allow us to express the k-space of the lower resolution image, $S[k_x, k_y]_{NxN}$, as:

$$S[k_x, k_y]_{NxN} = \sum_v \sum_w S[k_x + vN, k_y + wN]_{MNxMN};$$
$$-N/2 \leq |k_x, k_y| < N/2; \quad 0 \leq x, y < MN;$$
$$-M/2 \leq v, w < M/2 \qquad (4)$$

This is a truncation of a sum of shifted (aliased) copies of $S[k_x,k_y]_{MNxMN}$, the k-space of the original high-resolution data. This summation provides a theoretical explanation why, as a general observation, $S[k_x,k_y]_{NxN}$ (Eqn. (3), Fig. 1D) has higher amplitudes for high-frequency k-space components and lower regularity (smearing) of the low-frequency k-space components when compared to $S[k_x,k_y]_{EXPT}$ (Eqn. (2), Fig. 1B).

The impact of these differences is more clearly seen in the images where the summation operations introduce constructive and destructive interference between the superimposed aliased components of $S[k_x,k_y]_{MNxMN}$. Destructive interference in the aliased $S[k_x,k_y]_{MNxMN}$ that make up the $S[k_x,k_y]_{NxN}$ data leads to missing image components in the low resolution image $I[x,y]_{NxN}$, Fig. 1E, the inverse DFT of the Fig. 1D. Thus Eqn. (4) is the k-space expression of a MxM-fold decimation in the image domain of the high resolution image, $I[x,y]_{MNxMN}$ that keeps high resolution features located at positions $x=vM; 0 \le v < N$ and $y=wM; 0 \le w < N$. The blurring of the non NxN sparse lines in Fig. 1C compared to the sharpness of the NxN sparse lines in Figs. 1C and 1D can be interpreted as spatial leakage; the MR analogue of the spectral leakage described by Harris [4] when applying the DFT to finite length, time domain series.

b) Impact on under-sampling artefacts

A CS requirement is a k-space under-sampling scheme that produces aliasing artefacts in the image domain with a noise-like appearance (incoherent). Lustig's artefact analysis [1] involved k- space under-sampling schemes from a NxN Shepp-Logan phantom, which we have shown is comprised of components that are inherently NxN sparse. We extend this analysis to k-space data sets containing both NxN sparse and non-NxN sparse components.

A 1D DFT was applied to the upper and lower cross-sections of a $MNxMN$ HR image consisting of only the high-resolution lines of Fig. 1A to provide a data set equivalent to the Lustig et al. analysis. The k-space data corresponding to cross-sections of the lines of lower resolution NxN images produced by SDG-M1 and SDG-M2 simulation approaches were constructed. The frequency information of each cross-section was truncated to size $N= 32$, and frequency domain data sets reconstructed using a 1D $IDFT$ for (i) all, (ii) a 50% random and (iii) a 50% equi-spaced under-sampling of the k-space data; columns 1, 2 and 3 of Fig. 2 respectively. As with Lustig's analysis [1], we see aliasing artefacts
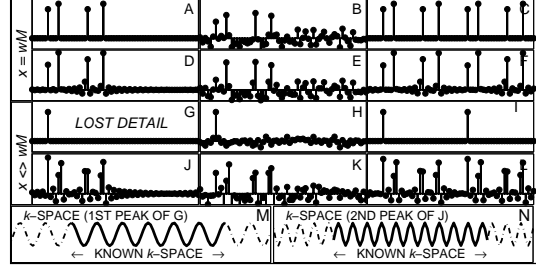

Fig. 2. The upper cross section (A) Cross section (Fig. 1, upper dotted dashed line) of the NxN Shepp-Logan phantom (Fig. 1E) has all HR detail centred at locations $x = wM; 0 \le w < N$. This section produces images (B) and (C) following random and equi-spaced k-space under-sampling. The same cross section derived from the truncated k-space data (Fig. 1B) is similar in appearance for reconstructions on full (D), random (E) and equi-spaced (F) under-sampled reconstructions respectively. A second cross section (lower dotted dashed line in Fig. 1) has most HR detail at locations $x \ne wM; 0 \le w < N$. Details are lost during the IDFT reconstructions of the NxN Shepp-Logan phantom calculated at resolution FOV / N from the full (G), random (H) and equi-spaced (I) under-sampled data sets. The truncated k-space data set retains detail following IDFT reconstruction from full (J), random (K) and equi-spaced (L) under-sampled data sets. (M) The first peak in (G) has k-space cyclic continuity [4] but (N) the second peak in (J) has no cyclic continuity

with a more noise-like appearance for a 50% random under-sampling scheme (column 2) than for 50% equi-spaced under-sampling (column 3) for data sets containing only N-sparse k-space components (SDG-M1, row 1; SDG-M2, row 2). A similar conclusion can also be reached for data sets having both N-sparse and non N-sparse components (SDG-M1, row 3; SDG-M2, row 4); but there are important differences in N and non N sparse reconstruction details.

1. There is a need to scale the SDG-M2 line images to match the peak intensities of the SDG-M1 line images; a reduction in fine detail intensity also seen clearly in the 2D $IDFT$ reconstructions, Figs. 1C and 1E.

2. For N-sparse under-sampled k-space data, the SDG-M1 and SDG-M2 data generation approaches generate similar, but not equivalent, image domain aliasing patterns, rows 1 and 2 respectively.

3. Differences exist between rows 3 and 4; the SDG-M1 and SDG-M2 line images containing both N-sparse and non-N-space components. The most obvious is the total loss of the non N-sparse image detail relative to the cross-sections of the original $MNxMN$ image for the SDG-M1 approach. Equally important in terms of possible impact on CS reconstruction success, is the changed characteristics of the noise artefacts, and the increased peak widths of the non N-sparse peaks, 2nd, 3rd and 4th peaks in Figs 2K and 2L.

c) Impact of CS reconstruction on k-space cyclic continuity.

The heavy lines in Figs. 2M and 2N are the 1D k-space data associated with the first peak in Fig 2G and the second peak in Fig. 2J respectively. Both 1D sets of known k-space data values (solid lines) are sinusoidal with a period reflecting the position of these peaks in their respective *NxN* and *MNxMN* images. The cyclic continuity [4] associated with these data sets has been empathized by generating copies of the data $S[k \pm N] = S[k]; \quad -N/2 \le k < N/2$; shown by the dashed lines. It can be seen that Fig. 2M shows complete k-space cyclic continuity (*N*-sparse), but there are amplitude and derivative discontinuities in Fig. 2N (non *N*-sparse).

Figs. 3A and 3C are again modifications of Fig. 1A; now representing image cross sections containing only *N*-sparse and non *N*-sparse fine lines respectively. The *IDFT* reconstruction of the truncated k-space data (dotted lines with open square markers appear blue in the on-line images) is sharp for the *N*-sparse lines in contrast to the wide peaks and ringing artefacts (spatial leakage) for the non *N*-sparse lines. Equivalent lines and markers in Figs. 3B and 3D respectively show the associated k-space data generated through a 1D *IDFT* of Fig. 3A and 3C. Again note the presence and absence of k-space cyclic continuity respectively present in the *N*-sparse (Fig. 3B) and non *N*-sparse image (Fig. 3D) components.

The vertical lines with round markers (appearing red on-line) in Fig. 3A and 3C are cross-sections of images from a 2D *IDFT* reconstruction of zero-filled, under-sampled, k-space data generated using the demonstration software from (2) and described in Section 3.1. Note the decreased signal-to-sampling-artefact ratio of Fig. 3C (SDG-M2) compared to Fig. 3A (SDG-M1) due to the wider, lower signal intensities of SDG-M2 lines (c.f. Fig. 2), combining with the increased level of artefacts associated with the spatial leakage of these non *N*-sparse k-space components.

The black lines in Fig. 3A and 3B show that a *CS* reconstruction on an *NxN* grid perfectly recovers the sharp peaks present in the image domain and all the missing k-space information for the naturally *N*-sparse data. In contrast, the black line in Fig. 3D shows that *CS* reconstruction has introduced cyclic continuity between locations $k_x = N/2 - 1$ and $k_x = -N/2$ by imposing a low-pass filter on the k-space data for the non *N*-sparse data. This CS imposed low-pass k-space filtering operation removes the rippling artifacts surrounding the main peaks in Fig. 3C, black line, but does nothing to aid the
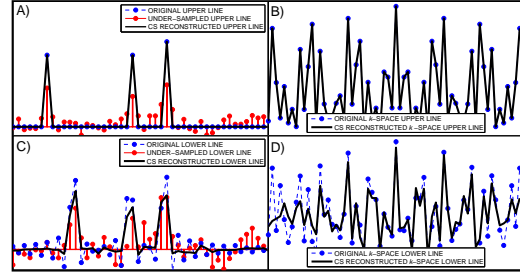

Fig. 3. A) and B) respectively show the image and k-space data of the upper cross section (dot-dashed line) of the original, under sampled, and CS reconstruction for the *NxN* Shepp-Logan phantom in Fig. 3. The upright lines with markers represent the cross-sections of the under-sampled reconstructions in Fig. 3. The dashed lines with markers representing the fully sampled reconstructions overlap the black lines of the CS reconstruction in A and B; indicating perfect recovery of the missing k-space data values. The k-space data in B) has perfect cyclic continuity. Different behaviour is demonstrated in C) and D) which respectively show the corresponding information for the lower cross section (dashed line) for the truncated k-space reconstruction. Although the ripples are reduced during CS reconstruction, dashed line with markers and black lines respectively in C), the peaks remain wider and lower in intensity than in A). Fig. D) indicates that the missing k-space values are better recovered for low k-space frequencies. The k-space data appears to have become windowed, low pass filtered, during CS reconstruction in order to meet Harris's cyclic continuity requirement (14) at locations $k_x = -N/2$ and $N/2 - 1$.

recovery of the lost peak intensities or sharpening the peaks (decreasing the peak width). We anticipate that use of a *Hi-KEE CS* reconstruction on a higher resolution grid, *PNxPN; P > 1,* will assist in the recovery of the resolution of the non *NxN* sparse features.

4.4 Comparing standard and *Hi-KEE* CS algorithms

Figs. 4(i) and 4(ii) compare results for *IDFT,* standard *CS* and *Hi-KEE CS* reconstructions from simulated and GE phantoms respectively. The figure format for each set of images is: *IDFT* reconstruction of (A) a zero-filled under-sampled (33%) truncated *64x64* k-space and (B) fully-sampled truncated *128x128* k-space. (C) A standard *64x64* CS reconstruction from an under sampled *64x64* k-space data set, a *x3* fold acceleration. (D) The *256x256 Hi-KEE* image from an under sampled *64x64* k-space data set is equivalent to approximately a *x50* fold acceleration on a *256x256* data acquisition. Images (E) and (F) are *256x256* and *512x512 Hi-KEE* reconstructions using 100% of the *64x64* k-space data, and 33% of the *128x128* k-space data respectively; corresponding to a *x16* and an *x24* acceleration on *256x256* and *512x512* data

acquisitions. Images A—C were pixel duplicated to size *256x256* to generate a common image size.

An image cross-section (G) compares the *NxN CS* reconstruction (dot-dashed line) and *4Nx4NHi-KEE* reconstructions (solid line) on 33% *NxN; N=64 k*-space data with the *IDFT* reconstruction of *2Nx2N* truncated data sets (dashed line). In image cross-section (H) the *IDFT* reconstruction on *2Nx2N k*-space values (dashed lines), *4Nx4N Hi-KEE* reconstruction on 100% *NxN; N=64 k*-space data (solid line) and *8Nx8N Hi-KEE* reconstruction on 100% *2Nx2N; N=64 k*-space data (solid line) are compared. The dotted and dashed lines in images (A) through (F) show the location of the upper and lower cross-sections used in (G) and (H).

• These cross-sections indicate that the *Hi-KEE* images have sharper edged features than *CS* reconstructions. However, while an improvement over the *CS* images, the *Hi-KEE CS* images using an 33% under-sampled *64x64 k*-space data set do not have the very fine detail present in the *IDFT* reconstruction of a *128 x 128* truncated data set (B). However applying the *Hi-KEE* approach to data sets larger than *64x64* significantly improves the image characteristics. The improvements on applying the *Hi-KEE* algorithm are particularly obvious with the GE phantom image's comb detail, located at the bottom of images in Fig. 4(ii). The same comb feature shows that the *512x512 Hi-KEE* reconstruction (F) of a 33% under-sampled *128x128* truncated data set is clearer than the *128x128 IDFT* reconstruction of the full *128x128* data set (B). This is because *k*-space continuity at, and *k*-space extrapolation beyond $| k_x |,| k_y | \approx N / 2; N = 128$, has been achieved during *512x512 Hi-KEE CS* reconstruction avoiding the hard *k*-space cyclic boundary window at associated with the standard *CS 128x128* image size.

The bottom row of images displays the absolute *k*-space values for Figs. (I) and (J) respectively and show *Hi-KEE CS* images from 33% under-sampled and all values of a truncated 64x64 *k*-space data set. Fig (K) provides the *512x512* (*8Nx8N*) *Hi-KEE CS* reconstruction on 33% of the *128x128* (*2Nx2N*) *k*-space values truncated from *k*-space of the highest resolution image decimated to size *256x256*. The central full and dotted rectangles show the extent of the original *64x64* (*NxN*) *k*-space values and the *k*-space border for *128x128* (*2Nx2N)* respectively. The *k*-space amplitudes for locations $| k_x |,| k_y | < N / 2$ are decreased in intensity by a factor of 2 to permit easier image comparison.

• Extrapolation beyond *128x128* (*2Nx2N*) is seen with all *Hi-KEE CS* reconstructions. Given there is

a significantly improved extrapolation for (J) the 100% *Hi-KEE* reconstruction over (I) the 33% reconstruction, additional extrapolation can also be anticipated following optimization of the *Hi-KEE* sampling scheme to account for the new higher-resolution. As this optimization will depend on image features, it will be more difficult to achieve than the approach used to optimize the point spread function of the *NxN k*-space sampling scheme implemented in [1]

The modified Shepp-Logan phantom, Fig. 5(i)J, shows strong *Hi-KEE CS* induced extrapolation to *4Nx4N* for many data features. Unfortunately, closer examination of the *k*-spaces of experimental *Hi-KEE* images shows that the accurate extrapolation of *k*-space is typically limited to a few points beyond $| k_x, k_y | > N / 2$ for complex image features. This implies that the *Hi-KEE* implementation has improved the resolution of the reconstructed non *NxN* sparse features beyond that found in Fig. 3D However, simply extending the *Sparse-MRI CS* objective function [1] to use a higher resolution grid preferentially encourages the retention of features of width *2p* and low intensity *q* rather than narrower features of width *p* and higher intensity *2q*. This implies that modification of the *Hi-KEE* implementations are needed to take full advantage of *CS* reconstruction at a higher resolution.

V Conclusion

We have demonstrated that the level of cyclic continuity present in *MR k*-space data affects the performance of compressed sensing (CS) algorithms. The *k*-space of the *NxN* images frequently used to validate the performance of *CS* algorithms have inherent *NxN* sparseness leading to ideal *k*-space continuity and perfect CS reconstruction of under-sampled data. This contrasts to experimental *MR* data with features that are both *NxN* sparse and non *NxN* sparse features having non identical resolution following *CS* reconstruction on an *NxN* grid. The *Hi-KEE CS* algorithm attempts to generate an image with a resolution closer to that of the original image rather than being limited to the gathered data size. The proposed *Hi-KEE* implementation improves the resolution of experimental *MR* data reconstruction above reconstructions on the standard *CS NxN* grid, but does not take full advantage of the available higher resolution.

Seaman MR Centre, University of Calgary, Dr. J. Miller, University of Alberta, Dr. H. Zhu, York University, and Dr. C. Song, Northeastern University, China.

REFERENCES

[1] M. Lustig, D. Donoho, J. M. Pauly. "Sparse MRI: the application of compressed sensing for rapid MR imaging", *Magnetic Resonance in Medicine*, 58(6):.1182-1195, 2007.

[2] Z. P. Liang, E. Boada, R.T. Constable, E. M. Haacke, P. Lauterbur, M. R. Smith. "Constrained Reconstruction Methods in MR Imaging", *Reviews of Magnetic Resonance in Medicine*, 4: 67- 18., 1992.

[3] G. McGibney, M. R. Smith, S. T. Nichols, A. Crawley. "Quantitative evaluation of several partial Fourier reconstruction algorithms used in MRI", *Magnetic Resonance in Medicine*, 30(1): 51-59, 1993.

[4] F. J. Harris. "On the use of windows for harmonic analysis with the discrete Fourier transform", *Proceedings of I.E.E.E.*, 66: 51 – 53, 1978.

[5] R. Van de Walle. H. H. Barrett, K. J. Myers, M.L. Aitbach, et al. "Reconstruction of MR images from data acquired on a general non-regular grid by pseudoinverse calculation", *I.E.E.E. Transactions on Medical Imaging* 19(12): 1160 – 1167, 2000.

[6] R. Chartrand. "Fast Algorithms for Nonconvex Compressive Sensing: MRI Reconstruction from Very Few Data", *International Symposium on Biomedical Imaging: From Nano to Macro*, 2009.

[7] M. Fuderer. "The information content of MR images", *I.E.E.E. Transactions on Medical Imaging* , 7(4): 368 – 380, 1988.
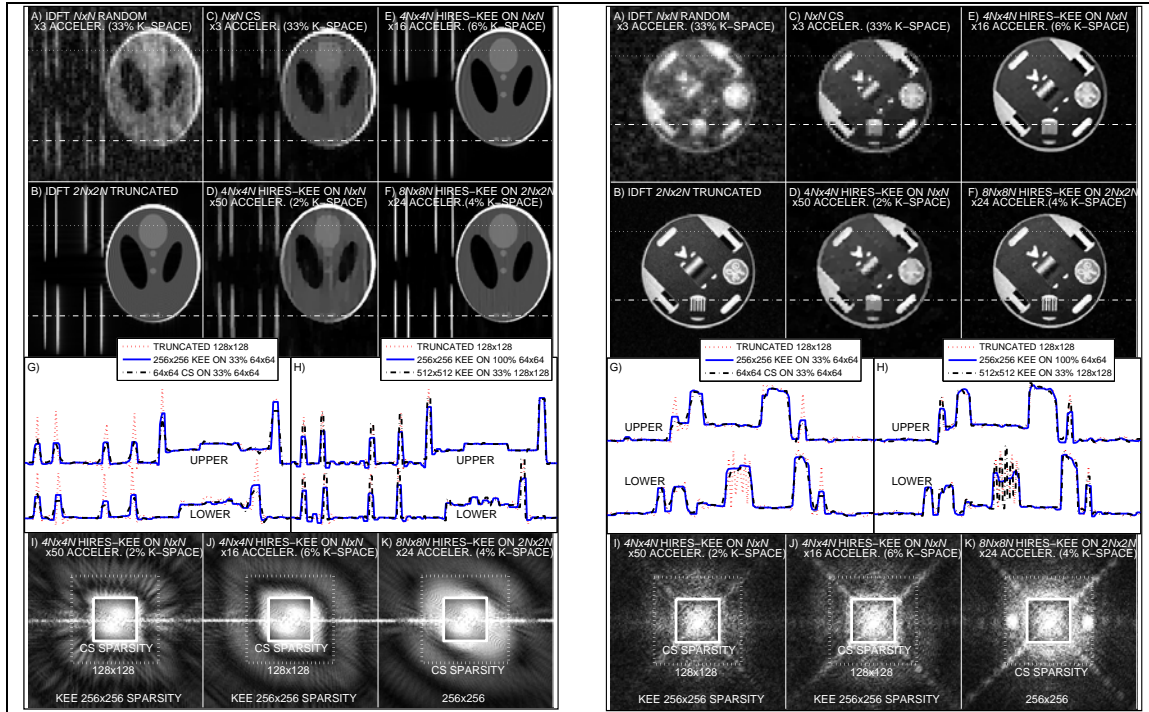
Fig. 4: *IDFT* reconstructed images from (A) sub-sampled selection (33%) from a *64x64 k*-space data set and (B) *128x128 k*-space data set truncated from a *2048x2048* Shepp-Logan phantom study in Fig. 5(i) and truncated from a *512x512 k*-space data set of a GE phantom in Fig.5(ii). (C) *64x64* CS reconstruction of 33% sub-sampled *k*-space, (D) *256x256 Hi-KEE CS* reconstruction of 33% sub-sampled *64x64 k*-space. (E) *256x256 Hi-KEE* CS reconstruction of 100% of *64x64 k*-space data and (F) *512x512 Hi-KEE* CS reconstruction of 33% % of *128x128 k*-space data 128x128. (G) shows cross-sections of images for a *128x128* IDFT reconstruction (dotted line), *64x64* CS reconstruction (dot-dashed line) and *256x256 Hi-KEE -CS* reconstruction (solid line) on *64x64* under-sampled truncated *k*-space values. Dotted and dashed lines indicate the position of the upper and lower cross sections in images (A) – (F). (H) shows cross-sections of images for a *128x128 IDFT* reconstruction (dotted line), *256x256* HI-KEE CS reconstruction (solid line) on 100% of *64x64 k*-space values and a *512x512 Hi-KEE* reconstruction on 33% of *128x128 k*-space values (dot-dashed line). *K*-space images are shown for *256x256 Hi-KEE CS* reconstructions on (I) 33% and (J) 100% of *64x64 k*-space data. (K) *512x512 Hi-KEE CS* reconstruction of 33% of *128x128 k*-space values. The *Hi-KEE* reconstructions on a high resolution *PNxPN* grid contain evidence of *k*-space extrapolation beyond the boundary of the original *k*-space values and standard *NxN CS* image grids.